

We are IntechOpen, the world's leading publisher of Open Access books Built by scientists, for scientists

6,900

Open access books available

186,000

International authors and editors

200M

Downloads

Our authors are among the

154

Countries delivered to

TOP 1%

most cited scientists

12.2%

Contributors from top 500 universities



WEB OF SCIENCE™

Selection of our books indexed in the Book Citation Index
in Web of Science™ Core Collection (BKCI)

Interested in publishing with us?
Contact book.department@intechopen.com

Numbers displayed above are based on latest data collected.
For more information visit www.intechopen.com



Thermal Microactuators

Leslie M. Phinney, Michael S. Baker and Justin R. Serrano
Sandia National Laboratories
USA

1. Introduction

This chapter discusses the design, fabrication, characterization, modeling, and reliability of thermal microactuators. Microelectromechanical systems (MEMS) devices contain both electrical and mechanical components and are in use and under development for applications in the consumer products, automotive, environmental sensing, defense, and health care industries. Thermal microactuators are standard components in microsystems and can be powered electrically through Joule heating or optically with a laser. Examples of MEMS designs containing thermal microactuators include optical switches (Cochran et al., 2004; Sassen et al., 2008) and nanopositioners (Bergna et al., 2005). Advantages of thermal microactuators include higher force generation, lower operating voltages, and less susceptibility to adhesion failures compared to electrostatic actuators. Thermal microactuators do require more power and their switching speeds are limited by cooling times.

Extensive work has been performed designing, fabricating, testing, and modeling thermal microactuators. Howell et al. (2007) has reviewed the fundamentals of thermal microactuator design. Designs of electrically powered MEMS thermal actuators include actuators fabricated from a single material (Comtois et al., 1998; Park et al., 2001; Que et al., 2001) and bimorphs (Ataka et al., 1993). Thermal actuator designs using a single material are both symmetric, referred to as bent-beam or V-shaped, structures (Baker et al., 2004; Park et al., 2001; Phinney et al., 2009) and asymmetric (Comtois et al., 1998), which have a hot arm and a cold arm. Asymmetric actuators are also referred to as flexure actuators. Some studies investigated both bent-beam and flexure actuators (Hickey et al., 2003; Oliver et al., 2003). In addition to electrical heating, powering thermal microactuators optically using laser irradiation has been demonstrated (Oliver et al., 2003; Phinney & Serrano, 2007; Serrano & Phinney, 2008). Modeling efforts have focused on bent-beam microactuators (Baker et al., 2004; Enikov et al., 2005; Howell et al., 2007; Lott et al., 2002; Wong and Phinney, 2007) and flexure actuators (Mankame and Ananthasuresh, 2001).

This chapter focuses on bent-beam and flexure microactuators. In order for thermal actuators to operate, sufficient heating and thermal expansion of the components must occur. However, device temperatures that are too high result in permanent deformation, damage, and degradation in performance. In addition, packaging processes and conditions affect the performance and reliability of microsystems devices motivating studies on the effects of surrounding gas pressure and mechanical stress on thermal MEMS.

2. Thermal microactuator designs

Figure 1 shows schematics of three thermal microactuator designs: bimaterial, bent-beam, and flexure. Bimaterial actuators consist of materials with different coefficients of thermal expansion and function similarly to a bimetallic thermostat (Ataka et al., 1993). When the temperature changes due to an embedded heater, the microactuator moves due to the difference in the expansion associated with the temperature change (Fig. 1a). Bent-beam

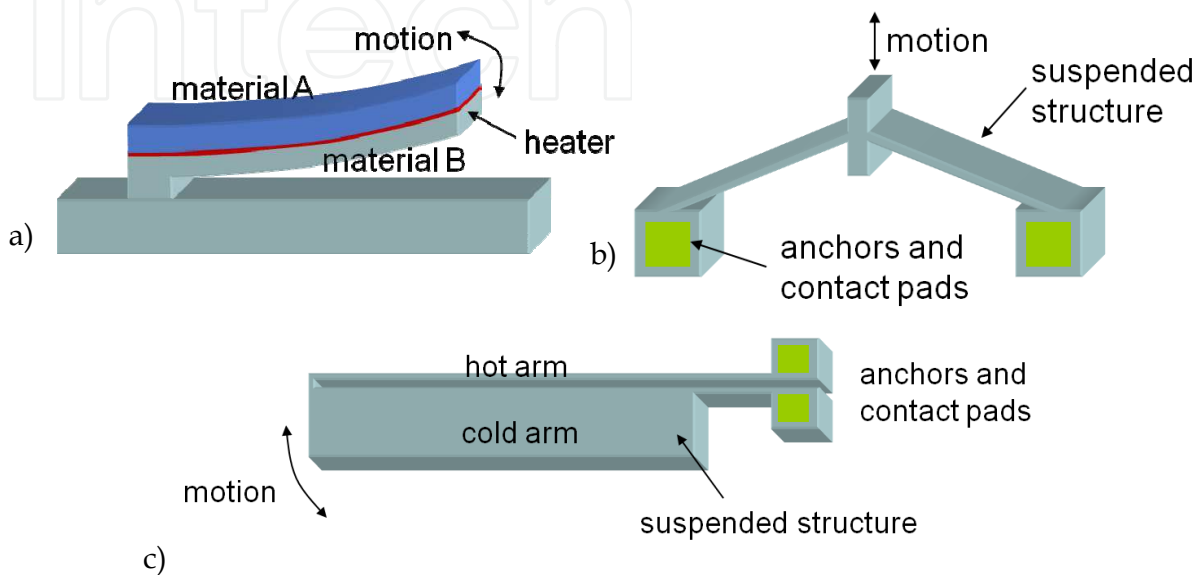


Fig. 1. Schematics of thermal microactuators: a) bimaterial, b) bent-beam, and c) flexure

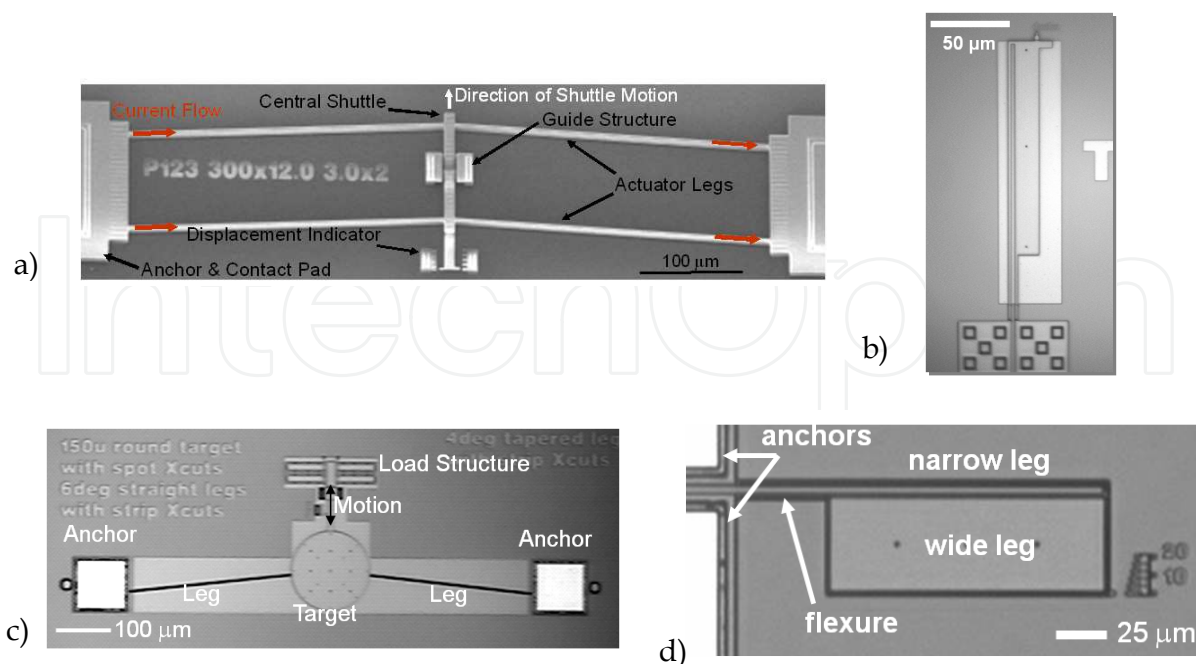


Fig. 2. Microscope pictures of thermal microactuators: a) electrically powered bent-beam, b) electrically powered flexure, c) laser powered bent-beam, and d) laser powered flexure

actuators have angled legs that expand when heated, providing force and displacement output as shown in Fig. 1b (Park et al., 2001; Que et al., 2001). The flexure actuator in Fig. 1c contains asymmetric legs, for example of unequal width, that flex to the side due to differential expansion when heated (Comtois et al., 1998). Figure 2 has pictures of electrically and optically powered bent-beam and flexure thermal microactuators.

3. Fabrication

Thermal microactuators are created using various microfabrication techniques including surface micromachining and silicon on insulator (SOI) processing which will be reviewed. Particular designs for surface micromachined thermal microactuators are presented in detail as characterization data for these designs are reported in Section 4.

3.1 Surface micromachining

Surface micromachining involves the sequential growth or deposition of thin films, patterning of features, and etching of the films to create multilayer structures and devices. Surface micromachining results in devices with in-plane dimensions from a few microns to millimeters and thicknesses of microns to 10 microns so they have low aspect ratios, i.e., thickness divided by length or width. Typical surface micromachining processes use polycrystalline silicon (polysilicon) for the structural layers and silicon dioxide for the sacrificial layers.

The surface micromachined thermal microactuators for which characterization data will be reported were fabricated using the SUMMiT V™ (Sandia Ultra-planar Multilevel MEMS Technology) process (Sniegowski and de Boer, 2000; SUMMiT V, 2008). The SUMMiT V process uses four structural polysilicon layers with a fifth layer as a ground plane. These layers are separated by sacrificial oxide layers that are etched away during the final release step. The two topmost structural layers, Poly3 and Poly4, are nominally 2.25 μm in thickness, while the bottom two, Poly1 and Poly2, are nominally 1.0 μm and 1.5 μm in thickness, respectively. The ground plane, Poly0, is 300 nm in thickness and lies above an 800 nm layer of silicon nitride and a 630 nm layer of silicon dioxide. The sacrificial oxide layers between the structural layers are each around 2.0 μm thick (Sniegowski and de Boer, 2000; SUMMiT V, 2008).

Figure 3 pictures schematics of an electrically heated bent-beam thermal microactuator with two legs and the cross-sectional area of an actuator leg with the width and thickness dimensions labeled. The SUMMiT V processing constraints on the sacrificial oxide cut between two polysilicon layers result in an I-beam shape for the thermal actuator legs (SUMMiT V, 2008). In this chapter, mechanical, electrical, and thermal characterization results are presented for bent-beam thermal microactuators with two actuator legs (Phinney et al., 2009). The thermal microactuator designs have the actuator legs fabricated from three laminated structural polysilicon layers: Poly1, Poly2, and Poly3 (Figure 4). This actuator design is referred to as the P123 actuator throughout this chapter. The second thermal actuator design is the same thermal actuator as the first design with a force gauge attached to the actuator shuttle (Figure 5) and is referred to as the P123F actuator. The force gauge consists of a linear bi-fold spring attached to the shuttle of the actuator using the Poly3 layer. Table 1 summarizes the geometries of the thermal microactuators with nominal

dimensions specified according to the SUMMiT V Design Manual (SUMMiT V, 2008). The shuttle that connects beams at the center is 10 μm wide, 100 μm long and its thickness is the sum of t_1 , t_2 , and t_3 .

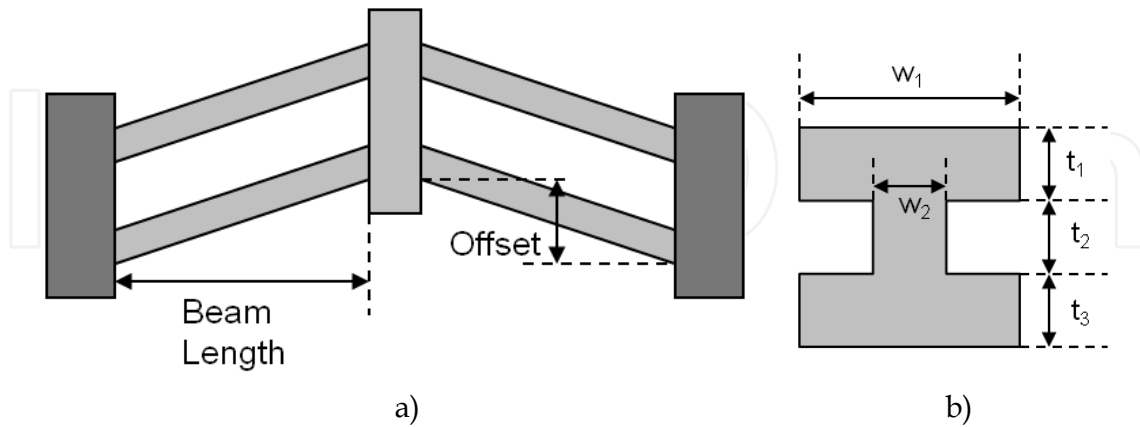


Fig. 3. Schematics of a) bent-beam thermal microactuator with two legs and b) actuator leg cross section showing dimensions that are specified in Table 1

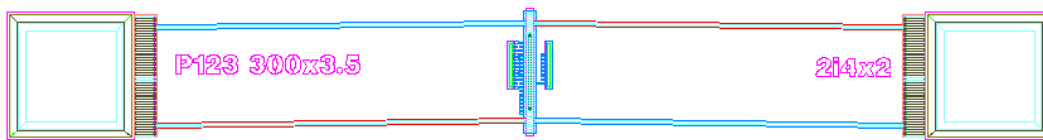


Fig. 4. P123 thermal microactuator schematic

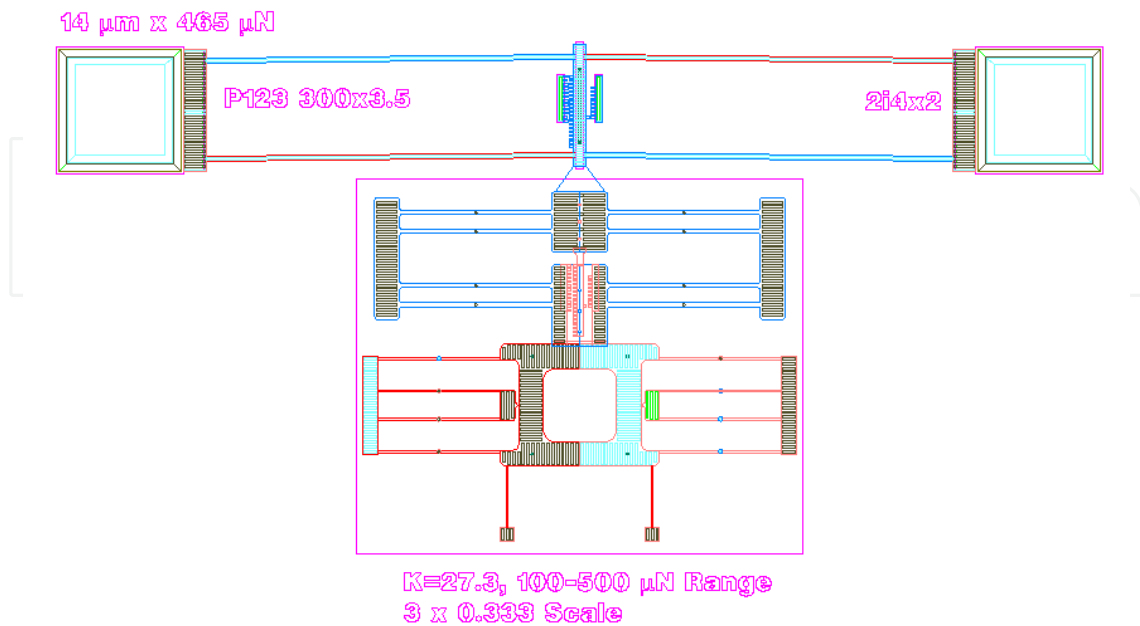


Fig. 5. P123F microactuator with an attached force gauge

Actuator	Gap to Substrate [μm]	Length [μm]	Offset [μm]	w_1 [μm]	w_2 [μm]	t_1 [μm]	t_2 [μm]	t_3 [μm]	Force Gauge
P123	2.0	300	3.5	4.0	2.0	2.5	2.0	2.25	No
P123F	2.0	300	3.5	4.0	2.0	2.5	2.0	2.25	Yes

Table 1. P123 and P123F thermal microactuator geometries

3.2 Silicon-on-insulator processing

A wide variety of microsystems devices such as microactuators, optical switches, accelerometers, and nanopositioners are fabricated with deep reactive ion etching (DRIE) using SOI (silicon on insulator) materials due to the high aspect ratios that can be achieved (Herrera et al., 2008). DRIE silicon etching is commonly referred to as Bosch etching and was patented by Lärmer and Schlip (1992). A thorough review of DRIE high aspect ratio silicon etching is presented by Wu et al. (2010). In SOI MEMS fabrication, the initial wafer has three layers: a single crystal silicon substrate wafer, a thin thermally grown silicon dioxide layer referred to as the buried oxide, and a mechanically thinned single crystal silicon layer called the device layer. A DRIE process enables high-aspect ratio, deep etching of features in silicon wafers using repeated cycles of conformal polymer deposition, ion sputtering, and chemical etching of the silicon. DRIE can be performed on both the device and substrate layers in order to pattern thermal microactuators from the device layer and remove the substrate underneath the microactuators (Milanović, 2004) to reduce heat loss and required power during operation (Skinner et al., 2008). Typically a metal layer is deposited on top of the device layer to improve electrical connections when the parts are packaged.

Example SOI thermal microactuator designs are pictured in Fig. 6 (Phinney et al., 2011). SOI thermal microactuators were fabricated from a wafer with: a 550 μm thick substrate, a 2 μm buried oxide layer, and a 125 μm thick device layer. Three bent-beam thermal microactuators were fabricated with four actuator legs having lengths from the anchor to the shuttle of 5500 μm or 7000 μm and leg widths of 50, 65, or 85 μm . During packaging, wires were bonded to the 0.7 μm aluminum layer that is deposited on top of the bond pad. Figure 6 shows a packaged die with the three thermal microactuators and bond wires visible.

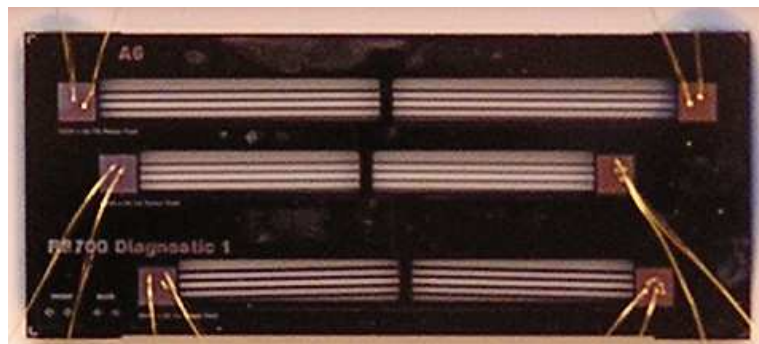


Fig. 6. Picture of SOI thermal microactuators. Two wires bonded to each bond pad are visible in the image. The square bond pads are 900 μm x 900 μm . The connections to the package are outside of the image.

4. Characterization

During operation of an electrically powered thermal microactuator, a current is applied to heat the actuator and thereby create displacement or force output. Displacement and total actuator electrical resistance measurements as a function of input current are easily obtained and standard metrics of thermal microactuator performance that are used for design comparison and model validation. Output force as a function of position and spatially resolved temperature measurements are additional performance and reliability metrics that are more challenging to obtain.

The displacement, electrical resistance, and force measurements in sections 4.1, 4.2, and 4.3 were performed according to methods described Baker et al. (2004). Displacement and total electrical resistance results were measured on a probe station using a National Instruments Vision software package that performs sub-pixel image tracking. A displacement measurement error of $\pm 0.25 \mu\text{m}$ was achieved by using 200X magnification. Force measurements were made using the P123F actuator design, in which a linear bi-fold spring is attached to the movable shuttle of the actuator. Force is applied manually to the actuator with a probe tip through the pull-ring attached to the spring. The displacement for a given force is determined from the vernier scale with $\pm 1/6 \mu\text{m}$ resolution. The applied force is determined from the measured displacements and calculated spring stiffness. This method of force measurement was used due to the lack of other methods viable for force measurements at this scale. The displacement, electrical resistance, and force measurements are compared to the results from a model which will be described in Section 5.

Temperature measurements were obtained using Raman thermometry (Kearney et al., 2006a; Kearney et al., 2006b; Phinney et al., 2009; Phinney et al., 2010a; Serrano et al., 2006). In the Raman process, photons from the incident probe light source interact with the optical phonon modes of the irradiated material and are scattered to higher (anti-Stokes) or lower (Stokes) frequencies from the probe line frequency. In the case of silicon and polysilicon, the scattered Raman light arises from the triply degenerate optical phonon at the Brillouin zone center. The resulting spectrum for the Stokes (lower frequency) Raman response has a single narrow peak at approximately 520 cm^{-1} from the laser line frequency at room temperature. Increases in temperature affect the frequency, lifetime, and population of the phonon modes coupled to the Raman process, leading to changes in the Raman spectra, including shifting the peak positions, broadening of the Stokes Raman peak, and increasing the ratio of the anti-Stokes to Stokes signal. These changes in the Raman spectra are metrics for temperature mapping of MEMS. Peak width is sensitive only to surface temperature, and peak position is sensitive to both stress and temperature (Kearney et al., 2006a; Beechem et al., 2007). The ratio of the anti-Stokes to Stokes signal tends to require the longest data collection time for quality signals. Since the thermal microactuators are free to expand and relieve stress that would affect the Raman signal prior to the measurement, Raman peak position is used for the Raman thermometry measurements in this section.

4.1 Displacement

Figure 7 shows the displacement versus applied current for the P123 thermal microactuator. The positive displacement from the designed zero location at zero current is due to compressive residual stress resulting from fabrication processes. The model results shown on the figures are for the thermomechanical model presented by Baker et al. (2004) and summarized in Section 5. When a bias is specified after "Model" in the legend, the bias

represents an edge bias which is subtracted from each side of thermal actuator leg nominal width. If a bias is not specified, the nominal width, $4.0\ \mu\text{m}$, is used in the model calculations. As the current is increased, the displacement versus current data exhibits an inflection point and roll-off in the curve. This is attributed to the maximum temperature in the thermal actuator legs becoming hot enough, above 550°C , that the polysilicon is softened or even melts (Baker et al., 2004). The thermal actuator legs have been observed to glow red under these conditions.

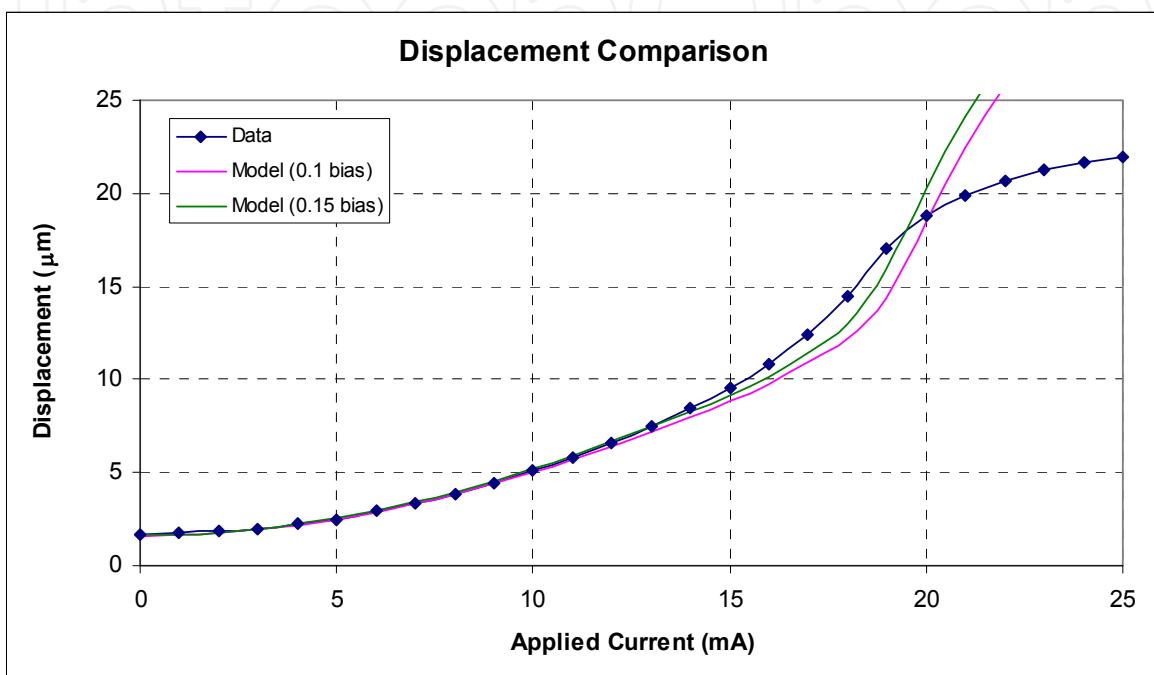


Fig. 7. Displacement versus current for the P123 thermal actuator

4.2 Resistance

Figure 8 shows the total electrical resistance for the actuators versus applied current for the P123 thermal microactuator. The resistance curve exhibits an inflection point, followed by a maximum, and then a decrease in resistance as the current is increased.

4.3 Force

Figure 9 shows the force for the P123F thermal actuator versus displacement when actuated at a constant current and voltage, 15 mA and 6.1V (Baker et al., 2004). For this test, the thermal actuator was held at a constant applied current and allowed to displace to its maximum unloaded position, which corresponds to the point on the graph where the curve intersects with the X-axis. Then using a probe tip, the force gauge was pulled away from the actuator, stretching the folded-beam spring in series between the probe tip and the actuator and applying a force to the thermal actuator center shuttle. The spring elongation was used to calculate the applied force and was recorded along with the actuator displacement. As the actuator is pulled back, the force increased to a maximum of $205\ \mu\text{N}$ at $\sim 6.75\ \mu\text{m}$. When pulled beyond this, the force begins to decrease due to buckling of the actuator legs. It is important to understand that this force curve represents the available output force of this single actuator design at this single applied power level. To fully characterize the force

output of an actuator design, a force curve would need to be measured at several different power levels. This family of curves would then map out the full force versus displacement behavior. The error bars shown for each force level were determined based on an uncertainty analysis performed on the spring design, taking into account the uncertainty in beam width, length, thickness, and Young's Modulus, as well as the measurement uncertainty in the spring elongation.

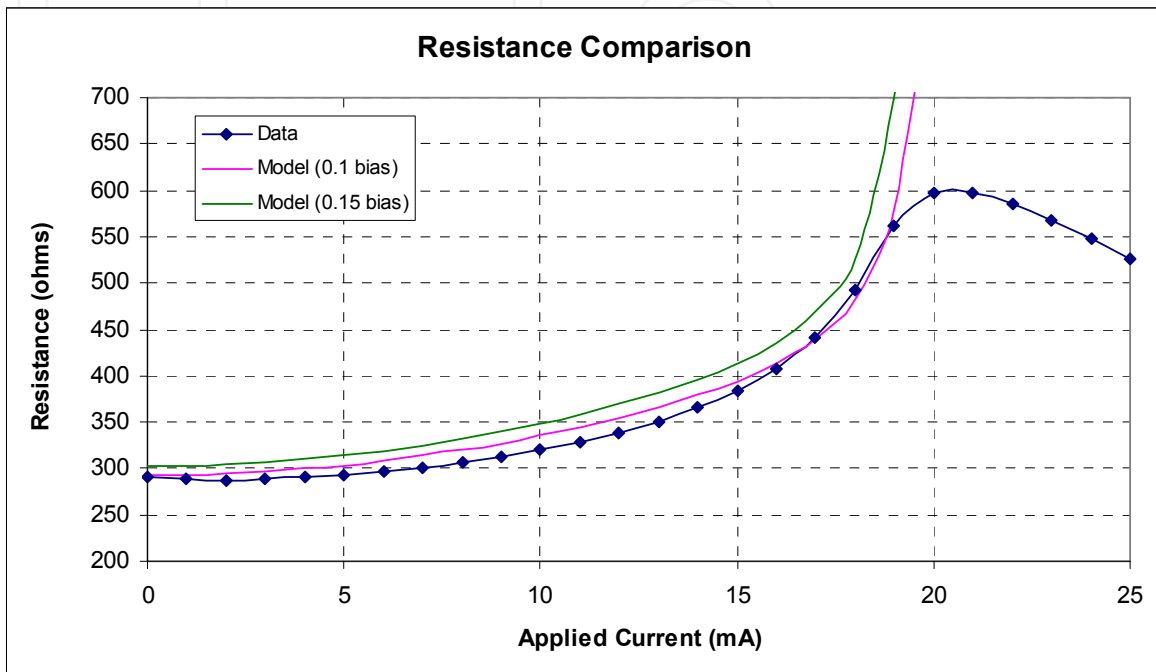


Fig. 8. Resistance versus current for the P123 thermal actuator

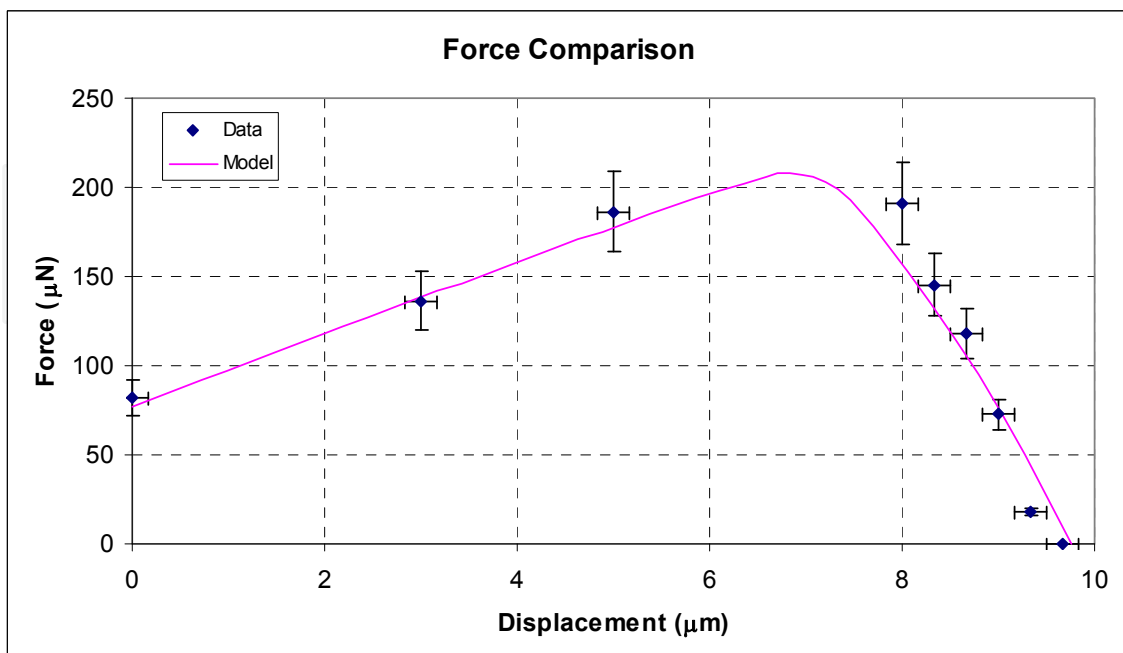


Fig. 9. Force versus position of the actuator at 15 mA for the P123F thermal actuator

4.4 Temperature measurements

Due to the challenges associated with obtaining spatially resolved temperature measurements on MEMS, thermal microactuator models have often been validated primarily from displacement and electrical measurements. Thermal microactuator performance depends on the temperatures of the microactuator legs. Experimentally measured temperatures are invaluable for understanding and improving thermal microactuator performance, model validation, and design optimization. Raman thermometry techniques were used to measure temperatures on electrically powered bent-beam thermal microactuators and laser powered flexure thermal microactuators.

4.4.1 Raman thermometry methods

Raman thermometry has been used to measure temperature profiles along the actuator legs of bent-beam and flexure thermal microactuators (Kearney et al., 2006a and 2006b; Serrano et al., 2006). Raman thermometry was performed using a Renishaw inVia Raman microscope. The microscope uses a 180° backscattering geometry and a 488 nm Ar⁺ laser as the probe that produces a diffraction-limited spot of 560 nm in diameter when focused by a 50×, 0.50-numerical-aperture objective. The actual measurement diameter within the sample is larger, 1.20 μm, because of spreading of the probe laser within the sample. The Raman signal from the sample surface is collected through the objective, dispersed by a grating spectrograph, and detected with a back-side illuminated, thermoelectrically cooled CCD camera (Princeton Instruments Pixis). Dispersion of the Raman signal at the CCD is 0.57 cm⁻¹/pixel.

Laser power at the sample is attenuated to minimize localized heating of the sample that would otherwise introduce a bias into the temperature measurement. Minimal heating of the sample is confirmed by obtaining Raman spectra at decreasing laser powers from a room-temperature sample until no change in the Raman peak position was observed. The 1.2 μm in-plane resolution of the Raman probe is capable of resolving widths of 2 μm to 4 μm for thermal microactuator legs. A detailed uncertainty analysis reveals that the reported Raman-measured temperatures are reliable to within ±10 to 11 K (Kearney et al., 2006a). These experimental results show that high-quality, reliable temperature measurements can be obtained. Most Raman thermometry measurements are performed when the devices are operating in a steady state in order to allow sufficient time for data collection with sufficient signal strength. Typical data collection times are on the order of tens of seconds to a few minutes. Transient measurements using periodic excitation are mentioned in Section 4.4.4.

4.4.2 Steady state electrically powered bent-beam thermal microactuator results

The temperature profiles reported in this section were taken using the Raman thermometry techniques reported by Kearney et al. (2006a, 2006b) and summarized in Section 4.4.1 on the surface micromachined actuators described in Section 3.1. Temperature measurements are made along one leg of the thermal microactuators starting from an anchor and ending at the center shuttle since the design and performance are symmetric. The chips with the P123 and P123F thermal microactuators were die attached and wire bonded in 24-pin Dual-in-Line Packages (DIP) that were inserted into a zero insertion force (ZIF) socket for the testing in laboratory air. The devices were powered with a Keithley 2400 Source Meter with a single lead on each anchor of the thermal microactuator.

Raman thermometry was used to measure temperatures along the lower left leg of P123 (four cases) and P123F (one case) thermal microactuators (Figure 10, Table 2). P123 microactuators on two packages, P5 and P6, were tested at two currents, 12 mA and 15 mA. The agreement between the temperature profiles for the P5 and P6 microactuators is within the experimental uncertainty of ± 10 to 11°C . Thus, the observed device-to-device variation is within the measurement uncertainty. As the current is increased from 12 mA to 15 mA, the maximum temperature increases significantly from 210°C to 377°C . The maximum temperatures along the microactuator legs occur at about two-thirds of the distance from the anchor to the shuttle. Since these tests were conducted at laboratory air pressures, heat transport from the shuttle to the cooler underlying substrate results in the shuttle acting as a heat sink. The temperature profile along a P123F microactuator leg (P5 F) at 12 mA decreases even more at the shuttle than for P123 microactuators tested at 12 mA due to the connection to the force gauge providing another pathway for energy transport away from the shuttle.

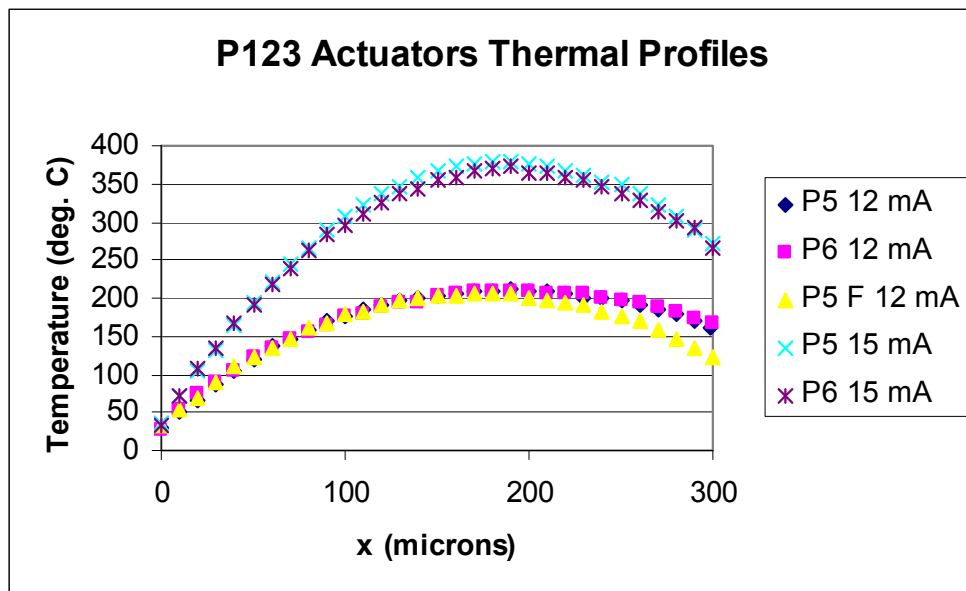


Fig. 10. Temperature profiles for the lower left leg of the P123 and P123F thermal actuators

Actuator	Current [mA]	Voltage [V]	Displacement [μm]	Maximum Temperature [$^\circ\text{C}$]
P123	12	3.89	6.67	210
P123	15	5.58	9.61	377

Table 2. Average actuator displacements, electrical measurements, and maximum temperatures at laboratory air pressure

4.4.3 Steady state laser powered flexure thermal microactuator results

Temperature measurements have also been made on laser heated polysilicon MEMS surfaces using Raman thermometry (Serrano and Phinney, 2008; Serrano et al., 2009; Serrano and Phinney, 2009). The Renishaw inVia microscope system was adapted to

accommodate a stage holding a 1:1 relay lens through which an 808 nm continuous wave fiber-coupled laser with a 100 μm core fiber could be focused on a MEMS part. This enabled temperature measurements on a thermal microactuator surface during laser heating. The heating laser was at an angle of incidence of 60° , yielding a $200\ \mu\text{m} \times 100\ \mu\text{m}$ elliptical spot on the surface. To avoid damage during measurement collection, a laser power of 314 mW was chosen. This power provides sufficient power to operate the device in a reliable fashion and avoid damaging the surface (Serrano and Phinney, 2008).

The flexure thermal microactuator was fabricated from using the SUMMiT V process and is pictured in Fig. 11a. The thermal microactuator was 200 μm long with a 2.5 μm wide \times 200 μm long narrow leg. The opposite side consisted of the 100 μm wide by 150 μm long Poly4 target and a 2.5 μm wide \times 50 μm long flexure element. The distance between the two legs was 5.0 μm . The full temperature profile of a 100 μm -wide Poly4 actuator was taken at 10 μm steps starting at the base of the narrow leg and down the near edge (the edge closest to the narrow leg) of the target surface and up to the base of the flexure element. The profile, shown in Fig. 11b, reveals that the temperature along both narrow elements (the thin leg and the flexure) increases linearly from the substrate temperature at the bond pads to the target surface temperature. On the target surface, the temperature in the near edge remains somewhat uniform from the point nearest the narrow leg up to the mid-length of the surface. Beyond this point, the temperature decreases as the flexure element is approached. The temperature profile in Fig. 11b differs from that for an electrically heated flexure thermal microactuator which has the highest temperatures in the narrow leg (Serrano et al., 2006). Since the target of the laser powered thermal actuator achieves the highest temperatures, the wide leg expands more than the narrow leg and the actuator curls in the direction of the narrow leg when powered. For an electrically heated flexure thermal actuator, the narrow leg will expand more than the wide leg and the actuator will move in the direction of the wide leg.

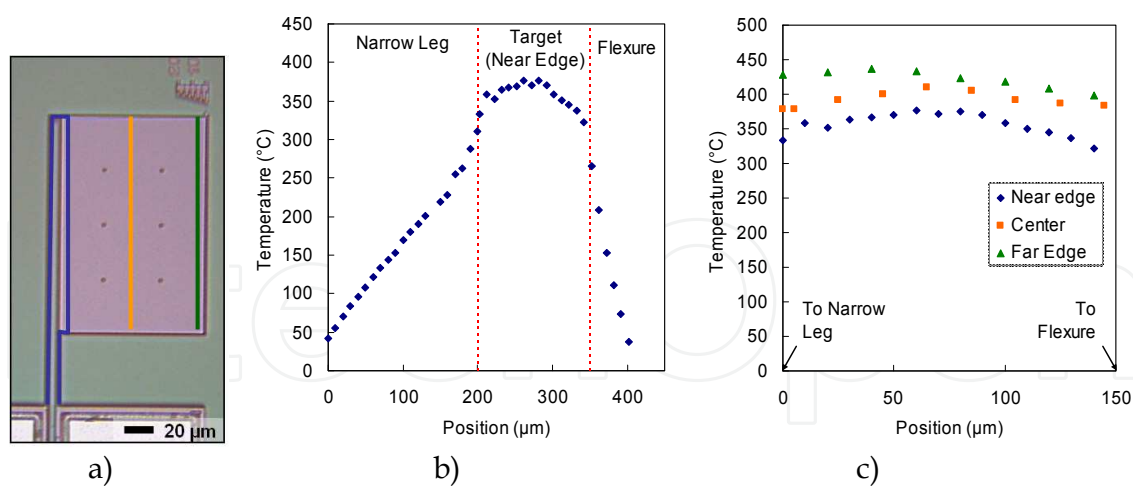


Fig. 11. Temperature profiles along a laser heated flexure actuator a) picture of flexure thermal microactuator and measurement paths, b) temperature profile along the near edge of the flexure actuator (blue line), and c) temperature profiles along the near edge, center, and far edge of the thermal microactuator target.

Comparing the profiles taken along the near, center and far edges of the target surface (Fig. 11c) reveals that the impact of the flexure element and the thin leg is most pronounced on the near edge. The presence of these elements results, on average, in average temperatures

$\sim 35^\circ\text{C}$ and $\sim 65^\circ\text{C}$ higher along the center and the far edge, respectively, than at the near edge. Moreover, temperature measurements reveal that the top-right corner of the target surface attains the highest temperature, $\sim 425^\circ\text{C}$. Subsequent measurements at varying laser powers revealed the effects of optical interference and temperature dependent optical properties on the peak temperatures (Serrano and Phinney, 2008; Serrano et al., 2009; Serrano and Phinney, 2009).

4.4.4 Transient bent-beam measurements

Raman thermometry usually requires data collection times on the order of tens of seconds to minutes to acquire sufficient signals from silicon and polysilicon thermal microactuators precluding transient measurements. Serrano and Kearney (2008) collected time resolved Raman thermometry measurements on polysilicon thermal microactuators using a phase-locked technique. They were able to achieve $100\ \mu\text{s}$ temporal resolution for a polysilicon two leg thermal microactuator design similar to a P123 microactuator but with $w_1 = 3.0\ \mu\text{m}$ and an offset of $12\ \mu\text{m}$ (Figure 3). Their measurements revealed that when the thermal microactuator is powered at $3.9\ \text{V}$ it achieved a maximum temperature of $\sim 150^\circ\text{C}$. The heating process took about $2\ \text{ms}$, and the thermal microactuator cooled in about $1.5\ \text{ms}$ after turning off the power.

5. Modeling

Numerous research groups have developed numerical models of thermal microactuator performance (Baker et al., 2004; Bergna et al., 2005; Enikov et al., 2005; Howell et al., 2007; Lott et al., 2002; Mankame and Ananthasuresh, 2001; Serrano et al., 2006; and Wong and Phinney, 2007). These models include electrical, thermal, and mechanical effects and are implemented through finite difference as well as finite element approaches.

An example of a model for thermal microactuators is the coupled electro-thermo-mechanical model that was developed to predict actuator performance (displacement, temperature and output force) as a function of the geometry and applied current (Baker et al. (2004)). The model utilizes a finite-difference thermal model to predict the total thermal strain at a given input current, accounting for temperature dependent material properties including thermal conductivity, electrical resistivity, and coefficient of thermal expansion. Heat conduction through the air gap into the substrate is included through the use of a conduction shape factor that is determined from a two-dimensional thermal analysis using the commercial finite-element analysis software ANSYS. Shape factors were determined to be 1.9856 for a $2.0\ \mu\text{m}$ gap between a P123 actuator and the substrate and 2.2336 for a gap of $2.8\ \mu\text{m}$. ANSYS is then used to model the structural response for the given thermal strain. This model is described in more detail by Baker et al. (2004).

The material properties used in the model include an electrical resistivity given by the following curve fit

$$\text{If } T < 300 \quad \rho = (2.9713 \times 10^{-2})T + 20.858$$

$$\text{If } T > 300 \text{ and } T < 700 \quad \rho = (6.1600 \times 10^{-5})T^2 - (7.2473 \times 10^{-3})T + 26.402 \quad (1)$$

$$\text{If } T > 700 \quad \rho = (8.624 \times 10^{-2})T - 8.8551$$

where the temperature is in degrees Celsius and the resistivity is in units of ohm-microns. The thermal conductivity is defined using the equation

$$k_p = \frac{1}{(-2.2 \times 10^{-11})T^3 + (9.0 \times 10^{-8})T^2 - (1.0 \times 10^{-5})T + 0.014} \quad (2)$$

where the temperature is in degrees Celsius and the thermal conductivity is in W/m/°C. At room temperature the thermal conductivity of polysilicon is 72 W/m/°C, and it decreases with increasing temperature. A value of 164 GPa was used for the Young's Modulus of polysilicon. The model curves in Figures 7-9 were calculated using this model. As seen in these figures, the predicted and measured displacements, electrical resistance, and force are in good agreement.

6. Reliability

The reliability of thermal microactuators depends on the packaging and environment as well as the initial design. Thermal microactuators have operated successfully for tens of millions of cycles; however, performance degradation mechanisms have been observed including plastic deformation of actuator legs, wear debris generation, void formation when operated in vacuum, changes in the grain structure, out of plane displacement, oxide growth, fracture of actuator legs, and die stress effects (Baker et al., 2004; Chu et al., 2006; Phinney et al., 2010b; Plass et al., 2004). Temperature measurements in reduced pressure environment and the effects of die stress are described in detail to illustrate the impact of environment and packaging on thermal microactuator performance.

6.1 Reduced pressure environments

Microsystems devices are often packaged at pressures lower than atmospheric, which dramatically affects the thermal performance of the parts since energy transfer to the environment is substantially reduced as the pressure is reduced (Phinney et al., 2010a). Thus, temperature measurements of thermal microactuators in varying pressures are crucial to optimizing device and package design as well as model validation.

Raman measurements were performed at nitrogen pressures varying from 0.05 Torr to 630 Torr using the Raman thermometry methods described in Section 4.3.1 and Torczynski et al. (2008). For reduced pressure measurements inside a Linkam thermal stage for which the pressure was controllable, a SUMMiT die with a P123 microactuator was packaged on a printed circuit board (PCB) to which wire leads were soldered. Each bond pad on the beam structure is wire-bonded to two separate connections on the PCB to allow for four-point sensing of the voltage. Quick-disconnect connectors were used inside the Linkam thermal stage to allow for easy exchange of parts. The PCB was placed in the center of a quartz crucible inside the stage and held in place with vacuum-compatible carbon tape. The heating ability of the stage was used to heat the sample to a temperature of 300-310 K to ensure a consistent substrate temperature for the measurements. The devices were powered with a Keithley 2400 Source Meter in a four-point sensing configuration, where the current is sourced through the outside connections and the voltage is measured across the inner ones.

Raman thermometry was used to measure the temperature profiles for a P123 microactuator leg at pressures ranging from 0.05 Torr to 630 Torr (Figure 12). In order to maintain similar

maximum temperatures in the P123 microactuator as the pressure reduced, the power applied to the microactuator was reduced as the pressure was decreased. The P123 microactuator power versus pressure is plotted in Figure 13. At pressures below about 5 Torr, the rate of decrease in the power to maintain the maximum temperature is less than at higher pressures as seen in Figure 13.

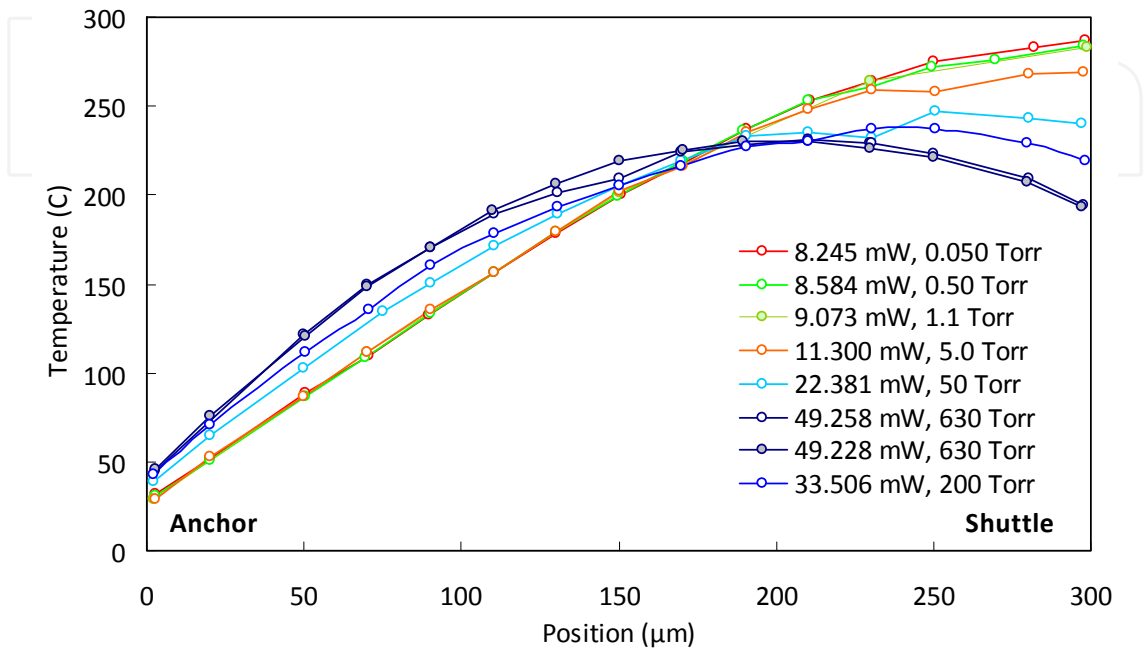


Fig. 12. Temperature profiles for a P123 microactuator leg at 0.05 to 630 Torr

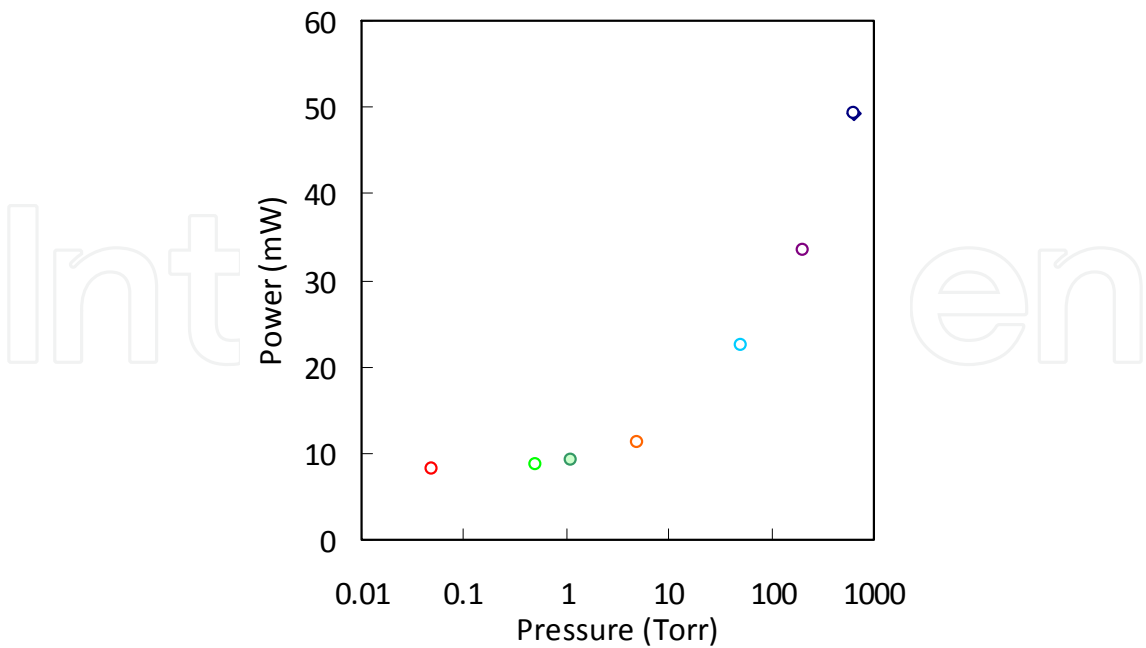


Fig. 13. Operating power for P123 thermal microactuator as a function of pressure for a constant actuator resistance

Pressure [Torr]	Current [mA]	Voltage [V]	Resistance [Ω]	Power [mW]	Displacement [μm]	Maximum Temp. [$^{\circ}\text{C}$]	Location of Maximum [μm]	Average Temp. [$^{\circ}\text{C}$]
0.050	4.910	1.67925	342.006	8.245	5.01	287	298.3	186
0.50	5.010	1.7133	341.976	8.584	5.01	284	297.9	185
1.1	5.150	1.76167	342.072	9.073	5.01	283	298.6	184
5.0	5.750	1.9653	341.791	11.300	5.01	269	297.6	182
50.0	8.090	2.7665	341.965	22.381	5.01	248	250.4	182
200	9.900	3.3844	341.859	33.506	5.01	238	230.4	182
630	12.000	4.1048	342.067	49.258	5.01	231	210.2	183
630	12.000	4.1023	341.858	49.228	5.01	230	210.2	184

Table 3. Actuator displacements, electrical measurements, location and magnitude of the temperature maxima, and average temperature under various nitrogen pressures

As seen in Figure 12, the location of the maximum temperature along the microactuator leg moves from around two-thirds of the distance from the anchor to the shuttle to the shuttle as the pressure is reduced. Heat transfer through the underlying gas from the microactuator to the cooler underlying substrate is significantly reduced as the pressure is decreased. At lower pressures, sufficient energy is not transferred from the shuttle to the substrate to allow the shuttle to maintain a lower temperature and act as a heat sink. The location of maximum temperature therefore moves from being on the microactuator legs at high pressures to being at the shuttle at the lower pressures. Table 3 summarizes the operating conditions used (pressure and current) as well as the voltage, resistance, power, displacement, magnitude and location of the temperature maximum, and the average temperature at the various pressures. It is important to note that, although the location and magnitude of the temperature maximum varies with pressure the length-averaged temperature, $\bar{T} = \frac{1}{L} \int T(x) dx$, remains fairly constant for all pressures, thus yielding the similar resistance and displacement values observed.

6.2 Effects of die stress

The effects of die stress were investigated by measuring thermal microactuator displacement as a function of applied current on a four-point bending stage for stresses ranging from -250 MPa compressive to 200 MPa tensile (Phinney et al., 2010b). Displacement as a function of both input current and applied external stress is shown in Figure 14 for three stress conditions corresponding to -18.7 MPa (the residual stress due to fabrication), 208 MPa tensile, and -261 MPa compressive. Increasing tensile stress decreases the initial displacement of the thermal microactuator, and the amount of displacement that occurs due to an applied current decreases when the device under test is subject to stress from the four-point bending stage.

The numerical model predictions using the model described in Section 5 agree qualitatively with the average of the experimentally measured displacements. The initial displacement decreases and the displacement curves flatten with increasing applied stress. Additionally, the calculated displacements agree with the experimental data for currents up to 25 mA. In Fig. 14, the predicted displacements were calculated for distances between the bottom of the thermal microactuator and the substrate of 2.0 μm and 2.8 μm . At 35 mA, the predicted

displacements using the nominal distance between the bottom of the thermal microactuator and the substrate of $2.0\ \mu\text{m}$ are significantly lower than the measured displacements for all three stress conditions. For the $-18.7\ \text{MPa}$ case with a gap of $2.0\ \mu\text{m}$, the predicted displacement is $14\ \mu\text{m}$ and the average of the measured values is $19\ \mu\text{m}$. Interferometric measurements at stresses of $-261\ \text{MPa}$, $-122\ \text{MPa}$, $-18.7\ \text{MPa}$, $115\ \text{MPa}$, and $212\ \text{MPa}$ showed that at currents starting at $20\ \text{mA}$ the thermal microactuator experiences upward out-of-plane displacement as well as forward displacement. The maximum measured out-of-plane displacement was $0.8\ \mu\text{m}$ at $35\ \text{mA}$ and occurred for the actuator at $-18.7\ \text{MPa}$. The upward deflection increases the underlying gap size under the center of the thermal microactuator. When the gap is increased to $2.8\ \mu\text{m}$ in the model, the predicted and measured thermal microactuator displacements are in good agreement. The remaining discrepancies are likely due to slight variations in the actuator geometry or material properties from nominal values.

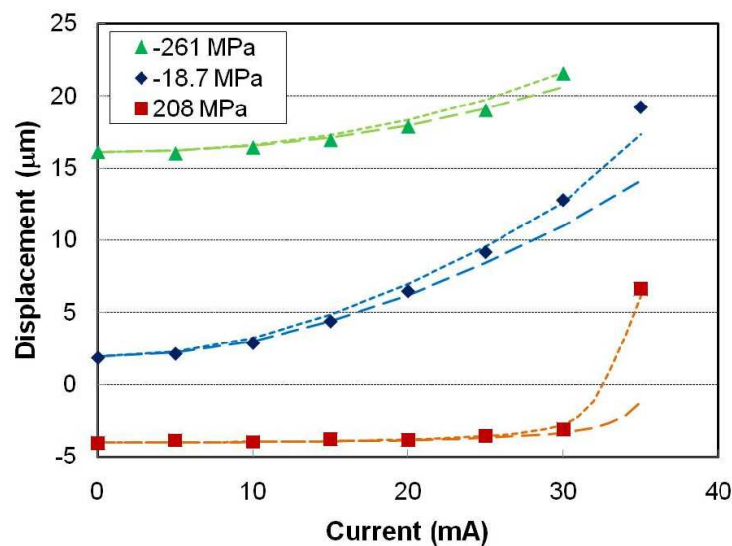


Fig. 14. Predicted and measured thermal microactuator displacement as a function of applied current. The symbols are the average of the experimentally measured displacements. The dotted lines represent the predictions for a gap between the bottom of the thermal microactuator and the substrate of $2.0\ \mu\text{m}$ (long dashes) and $2.8\ \mu\text{m}$ (short dashes).

7. Summary and conclusions

Thermal microactuators function due to thermal expansion of heated members and are versatile components for MEMS designs. Thermal microactuators are part of MEMS devices such as optical microswitches, nanopositioners, and microsensors. Two common thermal microactuator designs are the bent-beam actuator with angled legs that expand when heated and the flexure actuator with asymmetric legs that flex to the side due to differential expansion when heated. Thermal microactuators can be powered, heated, electrically or optically. Both surface micromachining and silicon on insulator (SOI) processing are used to fabricate MEMS thermal microactuators. In order to optimize the design, performance, and reliability of thermal microactuators, both experimental characterization and predictive modeling are necessary. Experimental measurements include displacement, electrical

resistance, force output, and temperature. Raman thermometry is a useful technique for acquiring spatially resolved temperature profiles along microactuator legs. The environment and packaging impact thermal microactuator performance and lifetime.

Thermal, electrical, and mechanical measurements for bent-beam polycrystalline silicon thermal microactuators are reported, including displacement, overall actuator electrical resistance, force, and temperature profiles along microactuator legs in standard laboratory air pressures and reduced pressures down to 50 mTorr. Typical displacements are up to around 15 μm with output forces of about 200 μN . For such devices, electrical resistances are in the 100s of Ohms and temperatures will increase by 100s of degrees Celsius. When operated in laboratory air, heating and cooling times are around 1-2 ms. Decreasing the pressure in which the thermal microactuators are operated moves the location of maximum temperature from about two-thirds of the distance between the anchor and shuttle to being on the shuttle. At low pressures, the shuttle does not function as a heat sink since it is not able to transfer the energy to substrate. Laser heated flexure actuators flex in the opposite direction as electrically heated flexure actuators and have the highest temperature at the corner of the wide leg target that is furthest from the flexure and narrow leg. Increasing tensile stress on bent-beam thermal microactuator samples decreases the initial displacement, and applied stress reduces the displacement output for applied currents.

8. Acknowledgment

Sandia National Laboratories is a multi-program laboratory managed and operated by Sandia Corporation, a wholly owned subsidiary of Lockheed Martin Corporation, for the U.S. Department of Energy's National Nuclear Security Administration under contract DE-AC04-94AL85000.

9. References

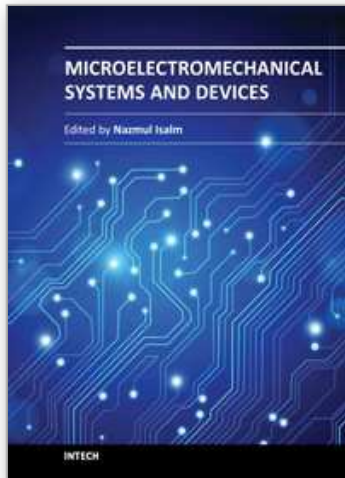
- Ataka, M.; Omodaka, A.; Takeshima, N. & Fujita, H. (1993) Fabrication and Operation of Polyimide Bimorph Actuators for a Ciliary Motion System. *Journal of Microelectromechanical Systems*, Vol. 2, pp. 146-150
- Baker, M. S. ; Plass, R. A. ; Headley, T. J. & Walraven, J. A. (2004) Final Report: Compliant Thermomechanical MEMS Actuators LDRD #52553, Sandia Report SAND2004-6635, Sandia National Laboratories, Albuquerque, NM
- Beechem, T.; Graham, S.; Kearney, S. P.; Phinney, L. M. & Serrano, J. R. (2007) Simultaneous Mapping of Temperature and Stress in Microdevices Using Micro-Raman Spectroscopy. *Review of Scientific Instruments*, Vol. 78, No. 6, Paper No. 061301, 9 pp.
- Bergna, S.; Gorman, J. J. & Dagalakis, N. G. (2005) Design and Modeling of Thermally Actuated MEMS Nanopositioners, *Proceedings of the 2005 ASME International Mechanical Engineering Congress and Exposition*, Paper No. IMECE2005-82158, 8 pp., Orlando, Florida, USA, November 5-11, 2005
- Chu, L. L.; Que, L.; Oliver, A. D. & Gianchandani, Y. B. (2006) Lifetime Studies of Electrothermal Bent-Beam Actuators in Single-Crystal Silicon and Polysilicon. *Journal of Microelectromechanical Systems*, Vol. 15, No. 3, pp. 498-506
- Cochran, K. R.; Fan, L. & DeVoe, D. L. (2004) Moving Reflector Type Micro Optical Switch for High-Power Transfer in a MEMS-Based Safety and Arming System. *Journal of Micromechanics and Microengineering*, Vol. 14, No. 1, pp. 138-146

- Comtois, J. H.; Michalicek, M. A. & Barron, C. C. (1998) Electrothermal Actuators Fabricated in Four-Level Planarized Surface Micromachined Polycrystalline Silicon. *Sensors and Actuators A*, Vol. 70, pp. 23-31
- Enikov, E. T.; Kedar, S. S. & Lazarov, K. V. (2005) Analytical Model for Analysis and Design of V-Shaped Thermal Microactuators. *Journal of Microelectromechanical Systems*, Vol. 14, pp. 788-798
- Herrera, G. V.; Bauer, T.; Blain, M. G.; Dodd, P. E.; Dondero, R.; Garcia, E. J.; Galambos, P. C.; Hetherington, D. L.; Hudgens, J. J.; McCormick, F. B.; Nielson, G. N.; Nordquist, C. D.; Okandan, M.; Olsson, R. H.; Ortiz, K.; Platzbecker, M. R.; Resnick, P. J.; Shul, R. J.; Shaw, M. J.; Sullivan, C. T. & Watts, M. R. (2008) SOI-Enabled MEMS Processes Lead to Novel Mechanical, Optical, and Atomic Physics Devices, *Proceedings of the 2008 IEEE SOI Conference*, pp. 5-8., New Paltz, New York, USA, October 6-9, 2008
- Hickey, R.; Sameoto, D.; Hubbard, T. & Kujath, M. (2003) Time and Frequency Response of Two-Arm Micromachined Thermal Actuators. *Journal of Micromechanics and Microengineering*, Vol. 13, pp. 40-46
- Howell, L. L.; McLain, T. W.; Baker, M. S. & Lott, C. D. (2007). Techniques in the Design of Thermomechanical Microactuators, In: *MEMS/NEMS Handbook: Techniques and Applications*, C.T. Leondes, (Ed.), 187-200, Springer US, ISBN 978-0-387-24520-1, New York, New York
- Kearney, S. P.; Serrano, J. R.; Phinney, L. M.; S. Graham, S.; Beecham, T. & Abel, M. R.; (2006a) Noncontact Surface Thermometry for Microsystems: LDRD Final Report, Sandia Report SAND2006-6369, Sandia National Laboratories, Albuquerque, NM
- Kearney, S. P.; Phinney, L. M. & Baker, M. S. (2006b) Spatially Resolved Temperature Mapping of Electrothermal Actuators by Surface Raman Scattering. *Journal of Microelectromechanical Systems*, Vol. 15, pp. 314-321
- Lärmer, F. & Schlip, A. (1992) Method of Anisotropically Etching Silicon, German Patent DE4241045 (1992) US Patent 5501893 (1996)
- Lott, C.D.; McLain, T. W.; Harb, J. N. & Howell, L. L. (2002) Modeling the Thermal Behavior of a Surface-Micromachined Linear-Displacement Thermomechanical Microactuator. *Sensors and Actuators A*, Vol. 101, pp. 239-250
- Mankame, N. D. & Ananthasuresh, G. K. (2001) Comprehensive Thermal Modelling and Characterization of an Electro-Thermal-Compliant Microactuator. *Journal of Micromechanics and Microengineering*, Vol. 11, pp. 452-462
- Milanović, V. (2004) Multilevel Beam SOI-MEMS Fabrication and Applications. *Journal of Microelectromechanical Systems*, Vol. 13, No. 1, pp. 19-30
- Oliver, A. D.; Vigil, S. R. & Gianchandani, Y. B. (2003) Photothermal Surface-Micromachined Actuators. *IEEE Transactions on Electron Devices*, Vol. 50, pp. 1156-1157
- Park, J.-S.; Chu, L. L.; Oliver, A. D. & Gianchandani, Y. B. (2001) Bent-Beam Electrothermal Actuators - Part II: Linear and Rotary Microengines. *Journal of Microelectromechanical Systems*, Vol. 10, pp. 255-262
- Phinney, L. M.; Epp, D. S.; Baker, M. S.; Serrano, J. R. & Gorby, A. D. (2009) Thermomechanical Measurements on Thermal Microactuators, Sandia Report SAND2009-0521, Sandia National Laboratories, Albuquerque, NM
- Phinney, L. M.; Lu, W.-Y. & Serrano, J. R. (2011) Raman and Infrared Thermometry for Microsystems, *Proceedings of ASME/JSME 2011 8th Thermal Engineering Joint*

- Conference Paper No. AJTEC2011-41462, 7 pp., Honolulu, Hawaii, USA, March 13-17, 2011
- Phinney, L. M. & Serrano, J. R. (2007) Influence of Target Design on the Damage Threshold for Optically Powered MEMS Thermal Actuators. *Sensors and Actuators A*, Vol. 134, pp. 538-543
- Phinney, L. M.; Serrano, J. R.; Piekos, E. S.; Torczynski, J. R.; Gallis, M. A. & Gorby, A. D. (2010a) Raman Thermometry Measurements and Thermal Simulations for MEMS Bridges at Pressures from 0.05 Torr to 625 Torr. *Journal of Heat Transfer*, Vol. 132, Article ID 0072402, 9 pp.
- Phinney, L. M.; Spletzer, M. A.; Baker, M. S. & Serrano, J. R. (2010b) Effects of Mechanical Stress on Thermal Microactuator Performance. *Journal of Micromechanics and Microengineering*, Vol. 20, Article ID 095011, 7 pp.
- Plass, R.; Baker, M. S. & Walraven, J. A. (2004) Electrothermal Actuator Reliability Studies, *Proceedings of SPIE: Reliability, Testing, and Characterization of MEMS/MOEMS III*, Eds. D. M. Tanner & R. Ramesham, Vol. 5343, pp. 15-21
- Que, L.; Park, J.-S. & Gianchandani, Y. B. (2001) Bent-Beam Electrothermal Actuators – Part I: Single Beam and Cascaded Devices. *Journal of Microelectromechanical Systems*, Vol. 10, pp. 247-254
- Sassen, W. P.; Henneken, V. A.; Tichem, M. & Sarro, P. M. (2008) An Improved In-Plane Thermal Folded V-Beam Actuator for Optical Fibre Alignment. *Journal of Micromechanics and Microengineering*, Vol. 18, No. 1, Article No. 075033, 9 pp.
- Serrano, J. R. & Kearney, S. P. (2008) Time-Resolved Micro-Raman Thermometry for Microsystems in Motion. *Journal of Heat Transfer*, Vol. 130, Article No. 122401, 5 pp.
- Serrano, J. R. & Phinney, L. M. (2008) Displacement and Thermal Performance of Laser-Heated Asymmetric MEMS Actuators. *Journal of Microelectromechanical Systems*, Vol. 17, No. 1, pp. 166-174
- Serrano, J. R. & Phinney, L. M. (2009) Effects of Layers and Vias on Continuous-Wave Laser Heating and Damage of Surface-Micromachined Structures. *Journal of Micro/Nanolithography, MEMS, and MOEMS*, Vol. 8, No. 4, Article ID 043030, 7 pp.
- Serrano, J. R.; Phinney, L. M. & Kearney, S. P. (2006) Micro-Raman Thermometry of Thermal Flexure Actuators. *Journal of Micromechanics and Microengineering*, Vol. 16, pp. 1128-1134
- Serrano, J. R.; Phinney, L. M. & Rogers, J. W. (2009) Temperature Amplification during Laser Heating of Polycrystalline Silicon Microcantilevers due to Temperature-Dependent Optical Properties. *International Journal of Heat and Mass Transfer*, Vol. 52, pp. 2255-2264
- Skinner, J. L.; Dentinger, P. M.; Strong, F. W. & Gianoulakis, S. E. (2008) Low-Power Electrothermal Actuation for Microelectromechanical Systems. *Journal of Micro/Nanolithography, MEMS, and MOEMS*, Vol. 7, No. 4, Article Number 043025, 7 pp.
- Sniegowski, J. J. & de Boer, M. P. (2000) IC-Compatible Polysilicon Surface Micromachining. *Annual Review of Materials Science*, Vol. 30, pp. 299-333
- SUMMiT V™ Five Level Surface Micromachining Technology Design Manual, Version 3.1a (2008) Sandia Report SAND2008-0659P, Sandia National Laboratories, Albuquerque, NM

- Torczynski, J. R.; Gallis, M. A.; Piekos, E. S.; Serrano, J. R.; Phinney, L. M. & Gorby, A. D. (2008) Validation of Thermal Models for a Prototypical MEMS Thermal Actuator, Sandia Report SAND2008-5749, Sandia National Laboratories, Albuquerque, NM
- Wong, C. C. & Phinney, L. M. (2007) Computational Analysis of Responses of Micro Electro-Thermal Actuators, *Proceedings of ASME 2007 International Mechanical Engineering Congress & Exposition* Paper No. IMECE2007-41462, 9 pp., Seattle, Washington, USA, November 11-15, 2007
- Wu, B.; Kumar, A. & Pamarthy, S. (2010) High Aspect Ratio Silicon Etch: A Review. *Journal of Applied Physics*, Vol. 108, No. 5, Article Number 051101, 20 pp.

IntechOpen



Microelectromechanical Systems and Devices

Edited by Dr Nazmul Islam

ISBN 978-953-51-0306-6

Hard cover, 480 pages

Publisher InTech

Published online 28, March, 2012

Published in print edition March, 2012

The advances of microelectromechanical systems (MEMS) and devices have been instrumental in the demonstration of new devices and applications, and even in the creation of new fields of research and development: bioMEMS, actuators, microfluidic devices, RF and optical MEMS. Experience indicates a need for MEMS book covering these materials as well as the most important process steps in bulk micro-machining and modeling. We are very pleased to present this book that contains 18 chapters, written by the experts in the field of MEMS. These chapters are grouped into four broad sections of BioMEMS Devices, MEMS characterization and micromachining, RF and Optical MEMS, and MEMS based Actuators. The book starts with the emerging field of bioMEMS, including MEMS coil for retinal prostheses, DNA extraction by micro/bio-fluidics devices and acoustic biosensors. MEMS characterization, micromachining, macromodels, RF and Optical MEMS switches are discussed in next sections. The book concludes with the emphasis on MEMS based actuators.

How to reference

In order to correctly reference this scholarly work, feel free to copy and paste the following:

Leslie M. Phinney, Michael S. Baker and Justin R. Serrano (2012). Thermal Microactuators, Microelectromechanical Systems and Devices, Dr Nazmul Islam (Ed.), ISBN: 978-953-51-0306-6, InTech, Available from: <http://www.intechopen.com/books/microelectromechanical-systems-and-devices/thermal-microactuators>

INTECH
open science | open minds

InTech Europe

University Campus STeP Ri
Slavka Krautzeka 83/A
51000 Rijeka, Croatia
Phone: +385 (51) 770 447
Fax: +385 (51) 686 166
www.intechopen.com

InTech China

Unit 405, Office Block, Hotel Equatorial Shanghai
No.65, Yan An Road (West), Shanghai, 200040, China
中国上海市延安西路65号上海国际贵都大饭店办公楼405单元
Phone: +86-21-62489820
Fax: +86-21-62489821

© 2012 The Author(s). Licensee IntechOpen. This is an open access article distributed under the terms of the [Creative Commons Attribution 3.0 License](#), which permits unrestricted use, distribution, and reproduction in any medium, provided the original work is properly cited.

IntechOpen

IntechOpen